# Enhanced tensile yield strength in laser additively manufactured Al0.3CoCrFeNi high entropy alloy

Mohan Sai Kiran Kumar Yadav Nartu, Talukder Alam, Sriswaroop Dasari, Srinivas Aditya Mantri, Stéphane Gorsse, Hector Siller, Narendra Dahotre, Rajarshi Banerjee

# Enhanced tensile yield strength in laser additively manufactured $Al_{0.3}CoCrFeNi$ high entropy alloy

Mohan Sai Kiran Kumar Yadav Nartu[a,b], Talukder Alam[a,b], Sriswaroop Dasari[a,b], Srinivas Aditya Mantri[a,b], Stephane Gorsse[c,d], Hector Siller[a,e], Narendra Dahotre[b], Rajarshi Banerjee[a,b,*]

[a] Advanced Materials and Manufacturing Processes Institute, University of North Texas, Denton, TX 76207, USA
[b] Center for Agile and Adaptive Manufacturing (CAAAM) and Department of Materials Science and Engineering, University of North Texas, Denton, TX 76207, USA
[c] CNRS, ICMCB, UMR 5026, 33600 Pessac, France
[d] Bordeaux INP, ENSCBP, 33600 Pessac, France
[e] Department of Engineering Technology, University of North Texas, Denton, TX-76207, USA

ARTICLE INFO

*Keywords:*
Additive Manufacturing
Strenghtening Models
High Entropy Alloys
Atom Probe Tomography

ABSTRACT

A precipitation strengthenable high entropy alloy (HEA), $Al_{0.3}CoCrFeNi$, was processed via laser-based additive manufacturing (AM), using the laser engineered net shaping (LENS) process. The as LENS processed HEA exhibited twice the tensile yield strength, as compared to the conventionally arc-melted and solution treated HEA of the same composition, with a tensile ductility greater than 20%. Subsequent heat-treatments of the AM HEA alloy led to further enhancement of the yield strength while maintaining good tensile ductility. The microstructure of these AM alloys was investigated by coupling transmission electron microscopy (TEM) and atom probe tomography (APT). The near doubling of the yield strength in case of the as AM processed HEA samples, which were devoid of second phase intermetallic precipitates, has been rationalized based on the formation of nanometer-scale Al–Ni rich solute clusters due to the re-heating of the deposited layers during AM. The enhanced yield strength due to these solute clusters has been estimated using a simple cluster-dislocation interaction model involving the coherency strain fields of these nano-clusters. The even higher yield strength in case of the heat-treated AM HEA samples has been quantitatively rationalized employing precipitation strengthening models, based on nanometer scale $L1_2$ (gamma prime) precipitates.

## 1. Introduction

Alloys with four or more principal elements, wherein the relative concentration of each element is between 5 and 35 at% are termed High Entropy Alloys (HEAs) or Complex Concentrated Alloys (CCAs) [1]. This new class of alloys allows the exploration of central regions of complex multi component phase space. Though originally introduced as single phase systems by Yeh et al. [2] and Cantor et al. [3], many HEAs have been shown to form precipitate phases during solidification, or during subsequent thermo mechanical processing [4 7]. Due to the combined effects of high entropy, sluggish diffusion, lattice distortion, and cock tail effect, many HEA systems have been reported to have novel mi crostructures leading to unique mechanical properties [8 12]. Among the many HEAs, the $Al_xCoCrFeNi$ is one of the most widely investi gated HEA system, and is currently one of the better understood ones [13 17]. While Li et al. [18] reported that $Al_{0.3}CoCrFeNi$ with a single phase (fcc) micro structure has a remarkable shear resistance, Gwalani et al. [12] exploited the phase stability of various ordered precipi tates in the same alloy to achieve a range of tensile yield strengths from ~150 MPa to as high as 1800 MPa. Although notable efforts have been made by multiple groups in analyzing the mechanical response of this HEA including tensile loading [12 19], compression [20], nano indentation [21], and creep [22], all of them have been on convention ally processed material. In this paper we explore the use of additive manufacturing techniques for the processing of this HEA.

Additive Manufacturing (AM) has been identified as a revolution ary technology over wide range of industries [23]. AM of metals into near net shapes is particularly attractive to the metal industries as by avoiding the assembly of parts, eliminates the risk of cracking and em brittlement at the junctions, thereby improving the performance of the material for structural applications. AM also enables us to design and manufacture parts with complex shapes using the computer aided de sign (CAD) models [24]. Laser Engineered Net Shaping (LENS), a pow der fed laser additive manufacturing technique, is faster when compared

* Corresponding author at: Center for Agile and Adaptive Manufacturing (CAAAM) and Department of Materials Science and Engineering, University of North TexasDenton, TX-76207, USA.
*E-mail addresses:* rajarshi.banerjee@unt.edu, banerjee@unt.edu (R. Banerjee).

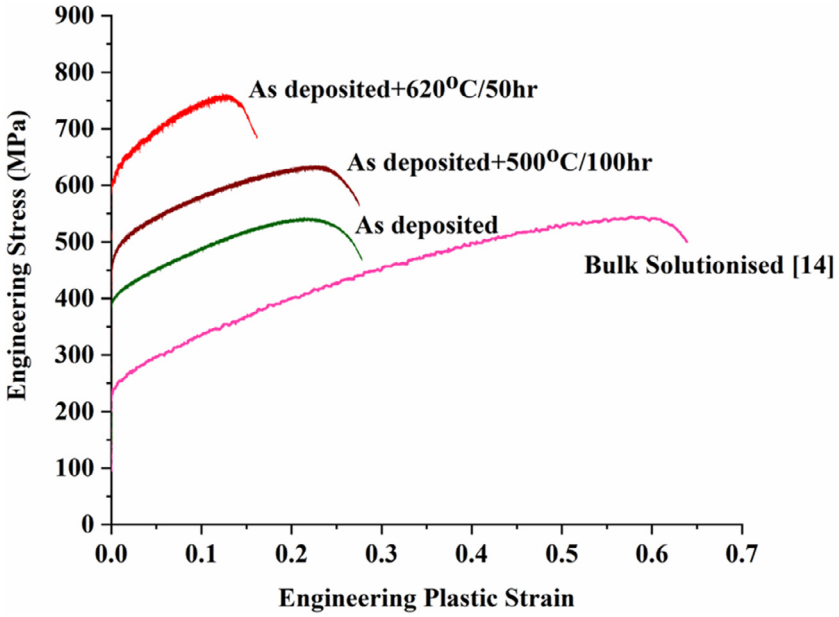


**Fig. 1.** Engineering stress-strain curves at room-temperature for $Al_{0.3}$CoCrFeNi HEA.

to other powder bed techniques, and the powder fed system employed renders the ability to functionally grade the material which is its unique feature [25].

Fujeida et al. [26] was among the first groups to demonstrate the use of selective electron beam melting method, an AM method, for AlCoCr FeNi HEA from the pre alloyed powders. The alloy showed a remark able increase in ductility and fracture strength compared to convention ally manufactured HEA. Harihar et al. [27] fabricated AlCoCrFeNi HEA via Laser Aided Direct Energy Deposition technique to study the effect of Al to Ni ratio and the subsequent phase evolution. However, they noted a few macro cracks at the substrate deposit interface that led to a poor quality build. The processing conditions play a vital role in de termining the build quality, which affects the mechanical properties. The material deposited undergoes complex heating and cooling cycles and this often leads to the formation of non equilibrium phases [28]. This in situ heat treatment occurring during the part building can be used to our advantage to minimize post processing [29 34]. A recent report on AM of CoCrFeMnNi, further illustrates the aforementioned ef fect on microstructure which resulted in enhanced mechanical strength [35]. Hence, AM could be potentially utilized to explore the properties of HEAs. This report investigates the structure property relationship of an additively manufactured and subsequently aged $Al_{0.3}$CoCrFeNi al loy. The unique microstructures contributing to the high strength were studied by high resolution microscopic techniques, Scanning Electron Microscope (SEM), Transmission Electron Microscope (TEM), and Atom Probe Tomography (APT).

## 2. Experimental procedure

An Optomec LENS 750 was used for processing $Al_{0.3}$CoCrFeNi HEA over a Ni substrate. A 1500 W Nd: YAG laser that produces near infrared radiation at a wavelength of 1.064 $\mu$m was used for the de position with a single powder hopper system loaded with the pre alloyed $Al_{0.3}$CoCrFeNi powder. The oxygen level in the glove box was maintained below 15 ppm during deposition. The processing pa rameters used were: 300 W laser power; 0.019″ (0.5 mm) laser beam size; 20 in/min (1.7 cm/s) laser scanning rate; layer spacing was 0.01″ (0.254 mm); hatch width was maintained at 0.015″ (0.381 mm) to make a 1″×1″×.5″ (25.4 mm×25.4 mm×12.7 mm) deposit. The deposited build was separated from the substrate and subsequently sliced into three sections using KENT USA (WSI 200) electric discharge machine (EDM). The heat treatments; 500 °C for 100 h and 620 °C for 50 h were performed on two of three sliced sections. The tensile specimens with gauge length ~ 5 mm, width ~ 1 mm and thickness ~0.7 1 mm were machined from the flat cross sections of the sliced sections i.e. perpen dicular to the build direction at a build height of 0.25″(6.35 mm). All the tensile tests were performed at a strain rate of $10^{-3}$ $s^{-1}$. At least three tensile specimens were tested for each condition and the plots with me dian values of tensile strength and ductility were reported.

SEM imaging for all the samples was done in FEI Quanta 200 ESEM and FEI Nova Nano SEM 230. Electron back scatter diffraction (EBSD) was performed in the FEI Nova Nano SEM 230 for grain size and resid ual stress measurement. Specimens for transmission electron microscopy (TEM) and Atom Probe Tomography (APT) studies were prepared in side a FEI Nova Nanolab 200 dual beam focused ion beam (FIB). TEM was carried out on a FEI Tecnai G2 F20 operating at 200 kV. APT ex periments were conducted on a CAMECA local electrode atom probe 5000XS instrument at a temperature of 30 K with a laser energy of 80pJ and 0.6 1.0% detection rate. APT data was reconstructed and analyzed by CAMECA IVAS® 3.8.2 software.

## 3. Results and discussion

The engineering stress strain curves from tensile testing of the three conditions are presented in Fig. 1. For comparison, the tensile data from bulk processed alloy [14] is also included in the same figure. The as de posited condition showed a yield strength (YS) of 410 MPa, whereas the conventionally processed and solution heat treated alloy from Gwalani's work was found to have a YS of ~220 MPa indicating a near two fold in crease in YS for the additively manufactured HEA. Subsequently, the AD HEA samples were further subjected to two different heat treatments; 500 °C for 100 h (hereafter referred to as AD 500) & 620 °C for 50 h (hereafter referred to as AD 620) based on a previous report [12]. The AD 500 and AD 620 conditions exhibited a YS of 500 MPa and 630 MPa and a ductility of 28% and 18%,% respectively.

SEM micrographs of AD, AD 500, and AD 620 conditions are shown in Fig. 2(a), (c) and (d), respectively. The AD condition did not reveal any secondary phases apart from the cell boundaries. The aged condi tions, AD 500 and AD 620 also revealed no second phase precipitates in the grain interior. However, a necklace of precipitates was observed along some grain boundaries in case of AD 620 condition, and will be discussed in detail, later in this article. For the AD condition, the grain

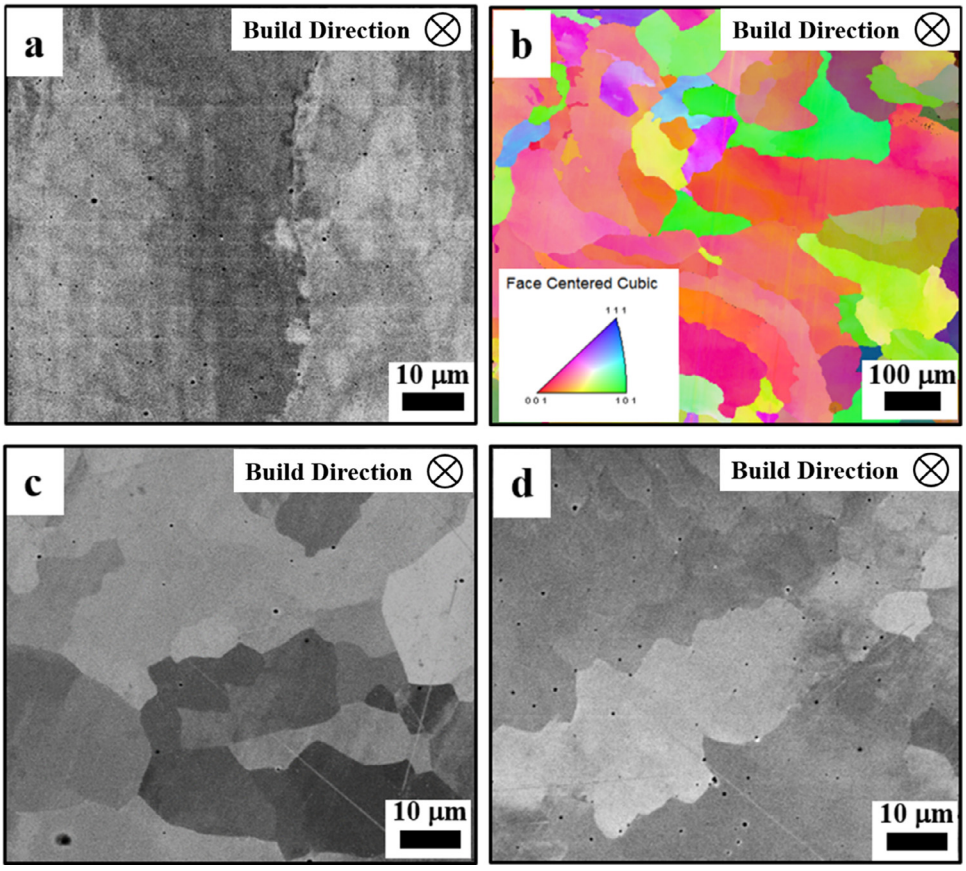


**Fig. 2.** Scanning electron micrographs (a) as deposited (AD), (b) IPF map of the AD alloy, (c) heat treated at 500 °C for 100 h (AD-500), (d) heat treated at 620 °C for 50 h (AD-620).

size distribution was measured by EBSD (Fig. 2(b)). The average grain size in the AD condition is ~50 μm. The previously reported average grain size for the conventionally processed (arc melted and solution treated) single phase HEA of the same composition was ~ 45 μm [14]. Therefore, the significant increase in tensile YS in case of the AD condition cannot be justified based on any change in grain size as compared to the conventionally processed HEA. The possible effect of residual stresses, as a result of AM processing, on enhancing the YS, was further analyzed by measuring the dislocation density in the AD condition. The distribution of the dislocations in the AD condition is shown in the bright field transmission electron microscope (BFTEM) image (Fig. 3). The average dislocation density measured from BFTEM images, recorded from at least three distinct regions, was $\sim 5 \times 10^{13}/m^2$. This value can be considered to lie in between the dislocation density of a fully recrystallized/annealed metallic alloy ($\sim 10^{11}/m^2$ [36]) and the typical dislocation density reported in case of selectively laser melted (SLM) alloy samples ($\sim 10^{14}/m^2$ [37]) . An additional factor that can result in a higher YS is the presence of fine scale cells or sub grain structures within the primary grains [38]. The cell boundaries can interact with the dislocations and result in the enhanced YS. Such cell boundaries have been shown in Fig. 2(a), with an average cell size ~5 $\mu$m. Since these cells are relatively coarse, their impact on the YS is expected to be rather small, but has been accounted for, in the overall strength model presented later in this paper.

Since AD 620 condition showed the highest strength, it was further investigated via TEM and APT. Fig. 4(a) shows the Selected Area Electron Diffraction (SAED) pattern obtained from the [111]fcc zone axis (ZA) of the AD 620 condition. Along with the fundamental FCC spots, super lattice reflections were clearly visible indicating the presence of a secondary $L1_2$ phase. Dark field (DF) image, in Fig. 4(b), obtained from $\frac{1}{2}$[0 22] spot revealed precipitates with two different morphologies. While the globular precipitates having a diameter of about 10 nm were distributed throughout the matrix, rod like precipitates with

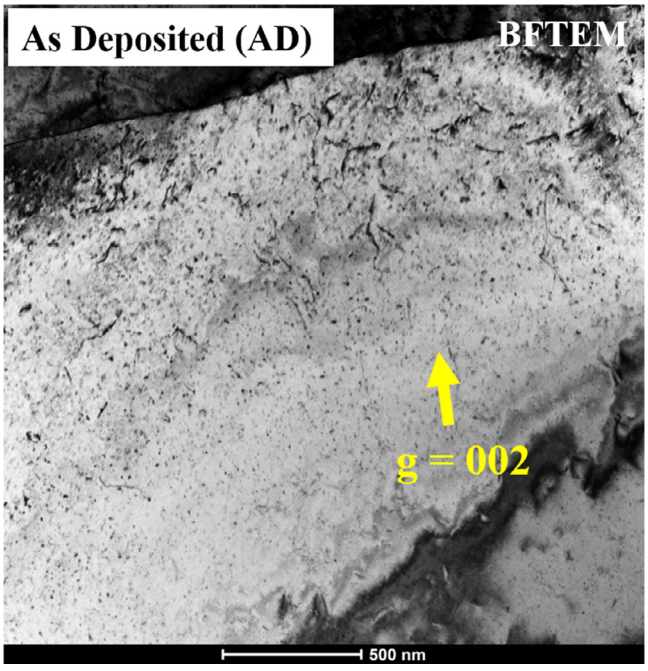


**Fig. 3.** BFTEM image showing the distribution of dislocations in the AD alloy.

a length and width of approximately 30 nm and 10 nm, respectively, were sparsely distributed in the matrix. In the HAADF STEM image in Fig. 4(c), two different morphologies of precipitates are observed again, and they are similar to those that have been previously reported [19].

APT was performed to determine the composition of these different phases. More importantly though, no signature of oxygen or nitrogen

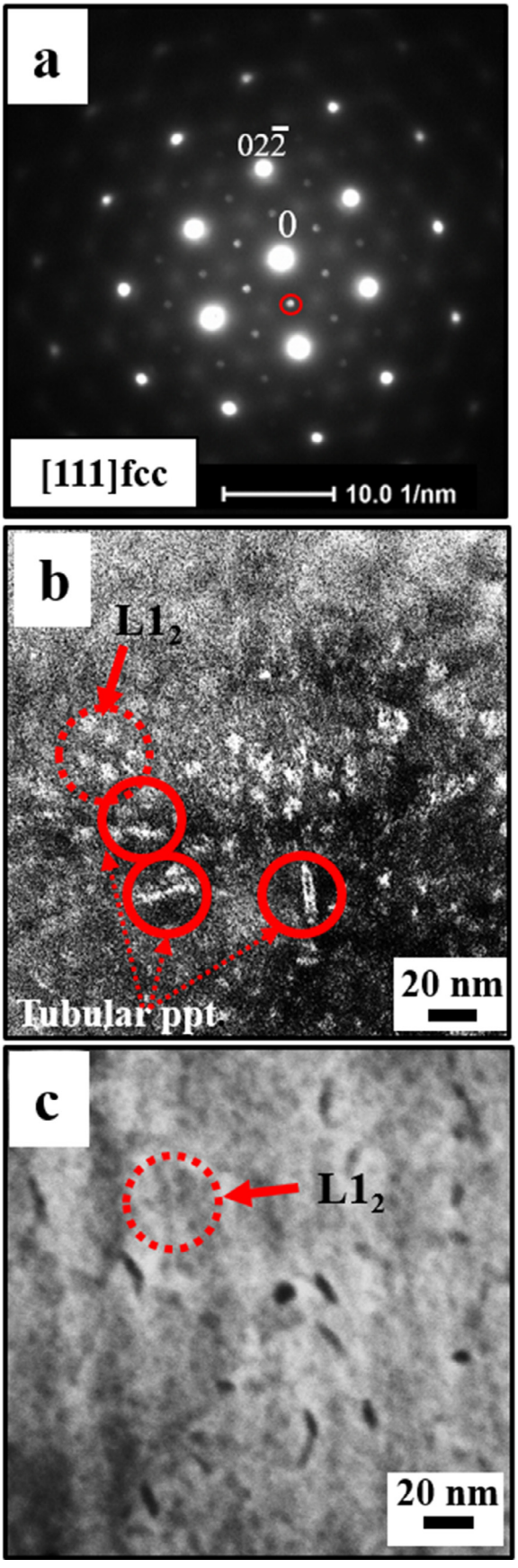


**Fig. 4.** AD-620 alloy (a) SAED pattern from [111]fcc ZA. (b) DF image obtained from the marked spot in (a), c) HAADF-STEM image of the matrix.

**Table 1**
Elemental composition of various ions in terms of at% of matrix and various precipitates from the AD-620 condition.

| AD-620 condition | | | | | | |
|---|---|---|---|---|---|---|
| Ion type | Matrix (fcc) | Error | Spherical ppt ($L1_2$) | Error | Rod-like ppt | Error |
| Al | 4.75 | 1.13 | 25.07 | 1.17 | 35.14 | 1.29 |
| Cr | 26.25 | 0.34 | 2.01 | 0.30 | 0.04 | 0.04 |
| Fe | 21.84 | 0.39 | 4.22 | 0.44 | 1.72 | 0.25 |
| Ni | 18.86 | 1.97 | 61.93 | 2.10 | 59.01 | 1.81 |
| Co | 27.25 | 0.46 | 6.41 | 0.55 | 3.66 | 0.36 |
| Mn | 0.61 | 0.09 | 0.23 | 0.10 | 0.14 | 0.07 |
| Si | 0.35 | 0.10 | 0.13 | 0.08 | 0.30 | 0.10 |
| Mo | 0.07 | 0.00 | 0.00 | 0.00 | 0.00 | 0.00 |

were detected above the background level of noise. Substitutional el ements like $O_2$and $N_2$ are believed to form undesired ordered precip itates [39] in HEAs and their absence certainly rules out their contri bution in enhancing the mechanical strength. A superimposed raw ion map of Al and Cr is shown in Fig. 5(a) and the segregation of these two ions is clearly visible. The discrete Al rich regions are the $L1_2$ precip itates whereas the Cr rich continuous region is the matrix. For visual clarity, iso surface (iso concentration surface) of Al 10% was used to distinguish the Al lean and Al rich regions and it is shown in Fig. 5(b) along with Cr ions. As described in the earlier section, two different morphologies are present in this alloy and they could be observed in this particular reconstruction. Near spherical $L1_2$ particles have a diam eter ranging from 5 nm to 10 nm. The rod like precipitate has a rather interesting 3D morphology. It has a length greater than 30 nm and as such only three precipitates were partially captured within the volume of the reconstruction. The cross section normal to the length of the pre cipitate is near oblong shaped; the shorter distance varies from 10 nm to 20 nm and maintains an aspect ratio with the larger distance of around 2. To check for the presence of any compositional difference between the precipitates, proxigram (proximity histogram [40]) could be utilized to show the average composition trend across the phase boundary. Two different sets of proxigrams were generated from the Al 10% iso surface shown in Fig. 5(b) from both morphologies of precipitates. Fig. 5(c) shows the proxigram plot (using five particles) from the spherical $L1_2$ phases while Fig. 5(d) shows plot from the three rod like precipitates. From the steady state values of the plots, it can be observed that the rod like precipitate has significantly higher level of Al (~11%) com pared to the spherical precipitate. The local composition of the precip itates was measured by placing a 3 nm diameter sphere and extracting a small volume from the interior of both the precipitates and they are listed in Table 1. The homogeneously distributed intra granular precip itates, predominantly of the $L1_2$ or $\gamma$' type, are expected to contribute to the high strength of the AD 620 alloy. While small differences can be observed in the levels of Ni, Cr, & Co, the major difference is in the Al concentration between these precipitates. The composition of the FCC matrix in case of the AD 620 condition is 4.75% Al 26.25% Cr 21.84% Fe 19.91% Ni 27.25% Co (at%), as shown in Table 1 and can be simpli fied as $Al_{0.17}CoCrFe_{0.8}Ni_{0.8}$.

While the matrix of the AD 620 alloy clearly showed these nanoscale precipitates, predominantly of the $L1_2$ or $\gamma$' type, the grain boundaries of this condition were also found to be decorated with larger precipitates, as shown in Fig. 6(a) in the back scattered SEM image. Based on pre vious reports on the bulk $Al_{0.3}CoCrFeNi$ alloy annealed at 620 °C/50 h, the grain boundary precipitates are likely to be Al rich B2 or Cr rich sigma ($\sigma$) phase [19]. STEM EDS was performed in the TEM to iden tify the precipitates based on the chemical composition. Fig. 6(b) shows the STEM image of the area selected for EDS scan and it incorporates three precipitates on a grain boundary. Elemental maps collected from the area are shown in Fig. 6(c) (e) for Al, Fe, and Cr, respectively. From this qualitative EDS analysis, it could be confirmed that both B2 and sigma ($\sigma$) phases are present on the grain boundary in this alloy.

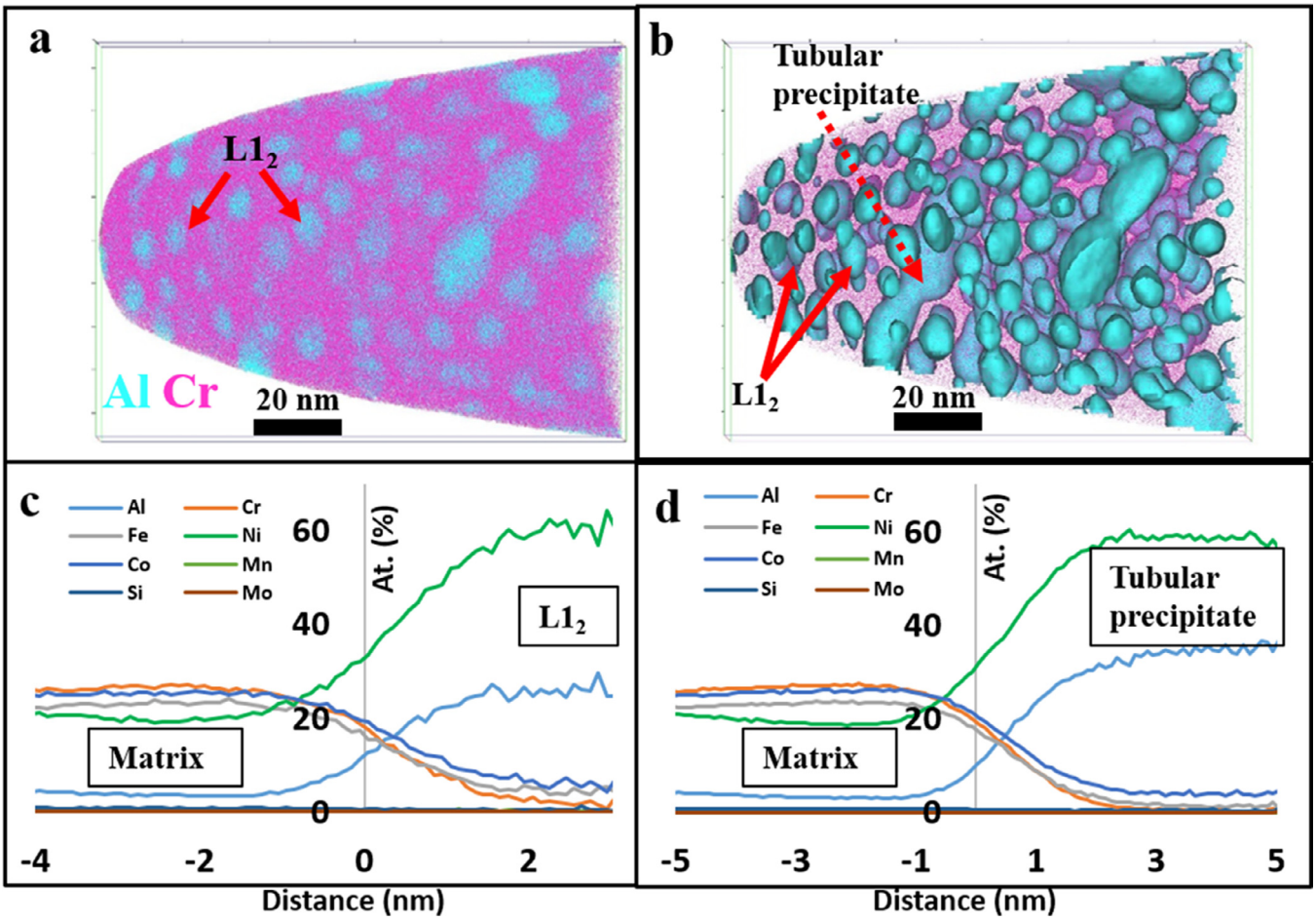


**Fig. 5.** AD-620 alloy (a) raw map of Cr and Al ions from APT, (b) iso-surface of Al-10% with Cr ions, (c) Proxigram across the interface between spherical $L1_2$ precipitate and the matrix. (d) Proxigram across the interface of rod-like precipitate and the matrix.

Similar to the aged alloy, TEM and APT analysis were also performed on the just as deposited (AD) alloy as it showed significantly higher strength values compared to the conventionally processed alloy of the same composition. The SAED patterns obtained from two different zone axes (ZA), [001]fcc and [011]fcc, did not reveal the presence of any su perlattice reflections, but just the fundamental spots. These are shown in Fig. 7(a) and (b). In the absence of any super lattice reflections it was determined that there are no secondary precipitates present in this alloy. Raw ion maps of Al and Cr obtained by APT are shown in Fig. 7(c) (d) and their uniform distribution further corroborates absence of secondary precipitates. From the mass spectrum the presence of distinct signature of $O_2$ or $N_2$ was not found above the noise level.

A (30 nm × 30 nm × 40 nm) region (Fig. 7(e)) from the reconstruction was then extracted to search for nano scale inhomogeneity. In the ex tracted volume several ions including Al and Ni were found to have a non random distribution. As such, they both were chosen as core ions for 'cluster hunting' routines in the IVAS software [41,42]. In total 232 (Al, Ni) rich clusters (Fig. 7(f)) were detected to have at least 162 core ions and an average volume of 32 nm$^3$. The average composition of these clusters is listed in Table 2. Previously it was also shown that these clusters acted as sources for pinning down the grain boundaries, con sequently hindering the grain growth in the $Al_{0.3}$CoCrFeNi alloy [43]. It is postulated that the high density of these (Al, Ni) rich clusters are the major contributors to the high strength of the as deposited alloy (AD condition) as they act as pinning sites for dislocation movements. Therefore, the influence of these (Al, Ni) rich clusters, within the FCC matrix, on the observed tensile strength of the AD sample needs to be assessed. Additionally, these clusters are believed to act as the heteroge

**Table 2**
Elemental composition of various ions in terms of at% of Al–Ni rich solute clusters from the AD condition.

| AD condition | | |
|---|---|---|
| Ion Type | (Al, Ni)-rich clusters | Error |
| Al | 14.20 | 1.80 |
| Cr | 14.19 | 1.72 |
| Fe | 12.22 | 1.59 |
| Ni | 44.48 | 2.60 |
| Co | 13.89 | 1.80 |
| Mn | 0.31 | 0.27 |
| Si | 0.68 | 0.44 |
| Mo | 0.03 | 0.09 |

neous nucleation sites for the subsequent $L1_2$ precipitation during aging at higher temperatures.

An attempt has been made to calculate the contributions of different strengthening mechanisms in case of both the AD and AD 620 samples. The Hall Petch contribution has been estimated based on the equations formulated by Gwalani et al. [14]:

$$\Delta\sigma_{HP} = 95 + \frac{824}{\sqrt{d}} \quad (1)$$

Based on an average grain size ~50$\mu$m for the AD sample, the Hall Petch contribution can be estimated to be approximately ~211 MPa. This accounts for ~50% of the observed YS. The strengthening

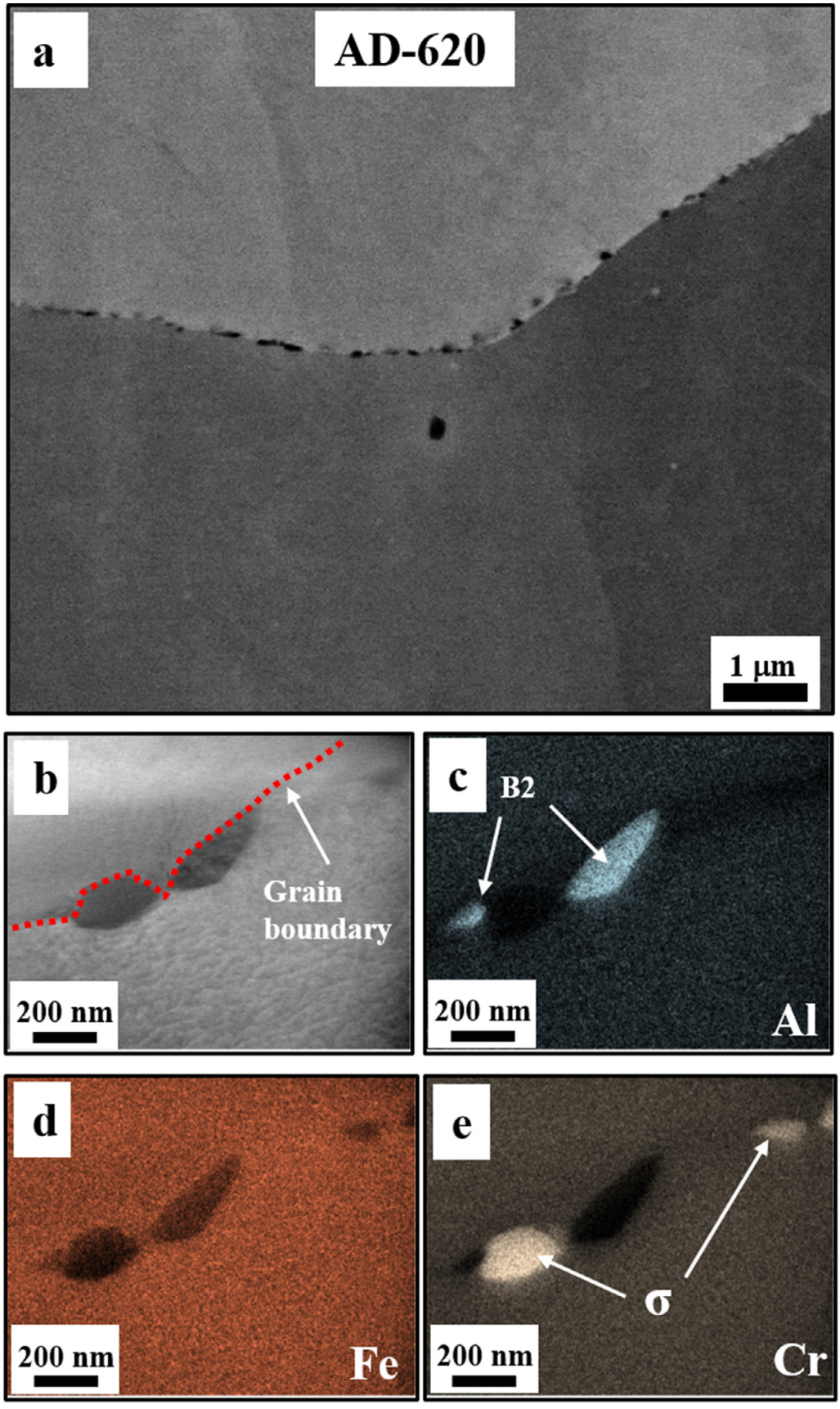


**Fig. 6.** AD-620 alloy (a) SEM image showing precipitates along a grain boundary. STEM-EDS images from a grain boundary. (b) The selected area for scanning. (c) Al map. (d) Fe map. (e) Cr map.

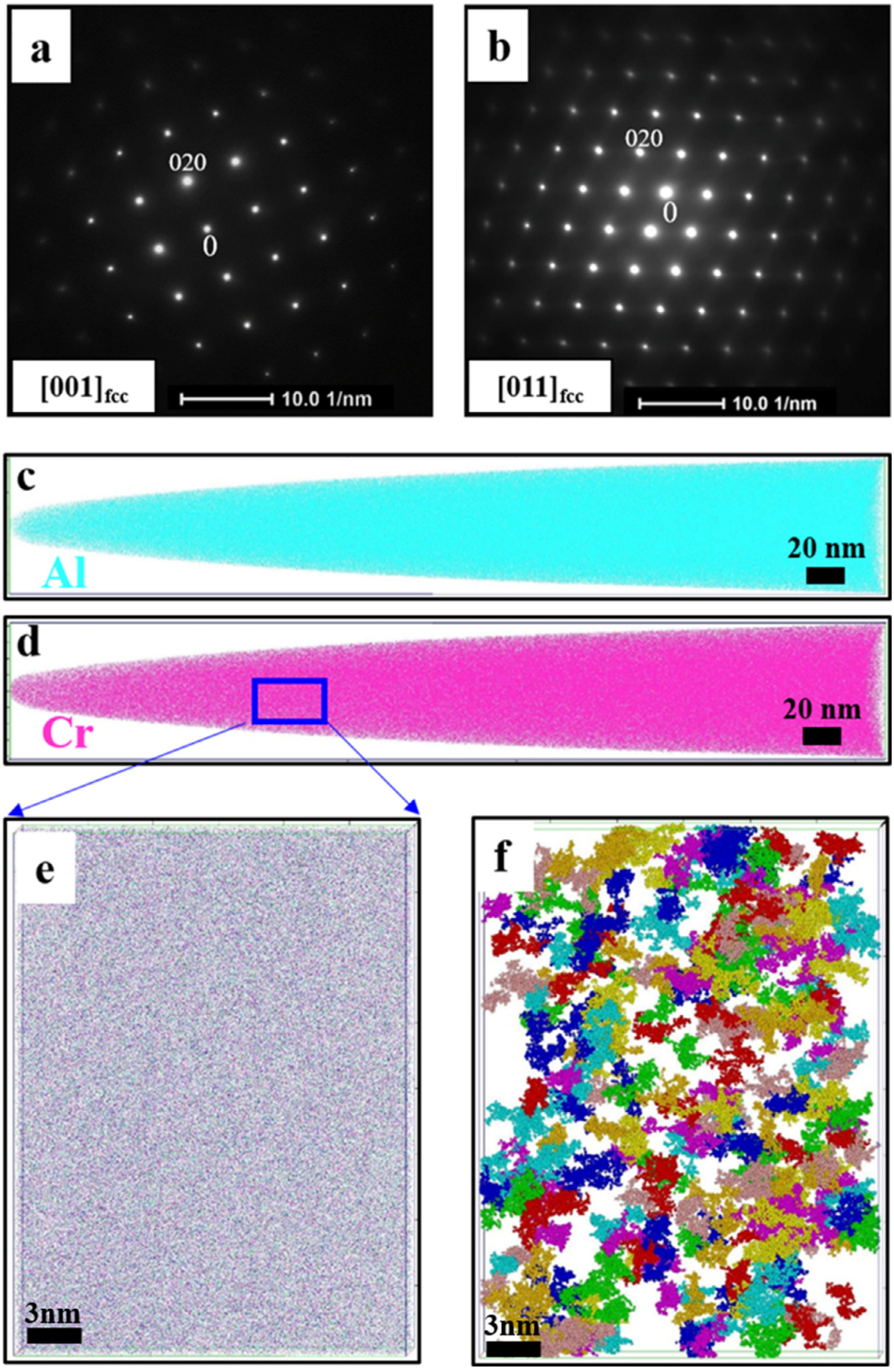


AD alloy (a) SAED pattern from [001]fcc ZA, (b) SAED patter from [011]fcc ZA, (c) raw ion maps of Al from APT, (d) raw ion maps of Cr, (e) extracted volume for cluster analysis, (f) (Al, Ni)-rich clusters inside the volume depicted in (e).

contribution from the sub grain cells with dislocation walls can be estimated by employing the following equation [38,44]:

$$\Delta\sigma_{cell} = MGb\sqrt{\rho} = \alpha MGb\left(\frac{c}{\lambda}\right) = \frac{\alpha c MGb}{\lambda} \quad (2)$$

*where,* $\alpha c = 1; M = 3.06; G = 80\,\text{GPa}; b = 0.255\,\text{nm};\ \lambda = 5\,\mu\text{m}$ (Intercellular Spacing)

All the values of the constants, used in the present calculations, are based on the CoCrFeMnNi alloy, which is closely related to the present system [44,45]. As mentioned earlier, the strengthening contribution of the sub grain cell boundaries ~12 MPa, is insignificant in comparison to the total YS ~410 MPa. The other possible factor that could lead to an enhancement in the yield strength is the dislocation density and its contribution to the yield strength which can be estimated using the following equation [46]:

$$\Delta\sigma_{disl} = AGb\sqrt{\rho} \quad (3)$$

*where, A is a constant ranging from* 0.3 *to* 0.6 *for various FCC metals*

$G = 80\,\text{GPa}; b = 0.255\,\text{nm}; \rho \sim 5\ \times 10^{13}/\text{m}^2$ $(dislocation\ density)$

Since the value of the constant A is not known for a complex FCC solid solution comprising four principal elements, the contribution of the dislocation density towards the yield strength of the AD alloy was estimated by assuming the entire range of possible A values from 0.3 to 0.6, corresponding to yield strength contributions ranging from ~43 MPa to ~86 MPa. Hence, the remaining contribution to the YS can be attributed to the presence of Al Ni rich clusters in the AD condition. The dislocation cluster interaction energy has been further analyzed in terms of stress required to overcome the coherency strain fields arising from these clusters. The strengthening contribution from coherency strains can be estimated using the following equations [12,47]:

$$\Delta\sigma_{Coherency} = 4.1G\varepsilon^{\frac{3}{2}}\sqrt{f}\sqrt{\frac{r}{b}} \quad (4)$$

*where,* $f = 0.18; r = 1.81\text{nm}; G = 80\text{GPa}; b = 0.255\text{nm},\ \varepsilon = 3.9\ \times 10^{-3}$

The values for volume fraction ($f$) and radius ($r$) of the clusters have been obtained from the APT analysis of samples from the AD condition. The misfit strain ε is calculated based on lattice parameter mismatch between matrix and the clusters by a simple Vegard's law approximation. Based on these, the following approximations were made:

$\Delta\sigma_{Coherency} = 90\text{MPa}$

Therefore, the total strength can be estimated by summation of individual contributions as shown below.

$$\sigma_{Total} = \Delta\sigma_{HP} + \Delta\sigma_{Cell} + \Delta\sigma_{Coherency} + \Delta\sigma_{disl}$$

$$\sigma_{Total} = 211\text{MPa} + 12.4\text{MPa} + 90\text{MPa} + [43 - 86\text{MPa}] = [356 - 399]\text{MPa}$$

The experimentally observed YS of 410 MPa is in reasonable agreement with the calculated values ranging from 356 MPa to 399 MPa, estimated on the basis of dislocation interactions with the coherency strain fields of the Al Ni rich clusters. This indicates that the in situ formed disordered Al Ni rich clusters, within the FCC matrix of the AD HEA, act as strain centers which interact with the dislocations during plastic deformation and result in an enhancement of the yield strength.

For AD 620 condition, the sub grain cell boundary strengthening contribution is assumed to be similar to AD condition because there is no change in the intercellular spacing with the heat treatment. Since there is a depletion of Al in the FCC matrix, after $L1_2$ precipitation, there is an overall change in the matrix composition, moving it more towards $Al_{0.1}$CoCrFeNi. The Hall Petch contribution of this composition can be estimated based on a previously reported equation for the $Al_{0.1}$CoCrFeNi alloy [48]:

$$\Delta\sigma_{HP} = 174 + \frac{371}{\sqrt{d}} \quad (5)$$

Based on the above equation, the Hall Petch contribution can be estimated as follows:

$\Delta\sigma_{HP} = 226\text{MPa}$

The strengthening contribution from is the shearing of the ordered $L1_2$ precipitates by the dislocations, can been estimated using the following equation [49]:

$$\Delta\sigma_{shearing} = 0.81M\left(\frac{\gamma_{apb}}{2b}\right)\sqrt{\frac{3\pi f}{8}} \quad (6)$$

*where,* $\gamma_{apb} = 198\frac{mJ}{m^2};\ f = 0.12; b = 0.255\text{nm};\ M = 3.06$

The value for the anti phase boundary energy used in the above calculation has been assumed to be similar to that of an $L1_2$ ordered phase whose composition is similar [50]. All other constants are based on the CoCrFeMnNi alloy. Volume fraction and radius of the precipitates (assuming spheres) have been estimated from the results of the APT investigations. Based on these approximations, the following strength enhancement values were calculated.

$\Delta\sigma_{shearing} = 361.8\text{Pa}$

The total YS can be approximated as follows:

$$\sigma_{Total} = \Delta\sigma_{HP} + \Delta\sigma_{Cell} + \Delta\sigma_{shearing}$$
$$= 226\text{MPa} + 12.4\text{MPa} + 361.8\text{MPa} = 600.2\ \text{MPa}$$

The total calculated yield strength, based on the shearing of ordered L12 precipitates model, is ~600 MPa, in close agreement with the experimentally observed YS of 630 MPa.

## 4. Summary

Summarizing, a detailed investigation of microstructure and strengthening mechanisms has been carried out on a precipitation hardenable high entropy alloy (HEA), $Al_{0.3}$CoCrFeNi, which has been processed via laser based additive manufacturing (AM), using the laser engineered net shaping (LENS) process. The nearly doubling of yield strength observed in the as deposited (AD) condition, as compared to the conventionally arc melted and solution treated HEA of the same composition, with similar grain sizes, could be rationalized based on APT results. It revealed the formation of nanometer scale Al Ni rich solute clusters due to re heating of the deposited layers during the LENS processing. The enhanced yield strength due to these solute clusters has been estimated using a simple cluster dislocation interaction model. These Al Ni rich clusters are believed to act as strain centers which interact with the dislocations during plastic deformation and result in an enhancement of the yield strength. Subsequent heat treatments of the AM HEA alloy (AD 620 and AD 500) led to further enhancement of the yield strength while maintaining good tensile ductility. The microstructure of the heat treated alloy (AD 620) investigated by coupling TEM and APT predominantly revealed nanometer sized $L1_2$ precipitates in the grain interior. The higher yield strength in this case (AD 620) has been quantitatively rationalized based on shearing of ordered $L1_2$ precipitates. The other strengthening contributions in both the conditions, AD & AD 620, such as grain boundary strengthening (Hall Petch) and strengthening from dislocations as well as sub cell walls have also been accounted for, in the calculation of the total yield strength.

## Declaration of Competing Interest

The authors declare that they have no known competing financial interests or personal relationships that could have appeared to influence the work reported in this paper.

## Acknowledgment

The authors acknowledge part financial support for this work from a seed research project funded by the Advanced Materials and Manufacturing Processes Institute (AMMPI) at the University of North Texas

(UNT), and from the U.S. Army Research Laboratory (ARL) funded Co operative Agreement W911NF 19 2 0011 at UNT. Additionally, the au thors also acknowledge the Center for Agile and Adaptive Manufactur ing (CAAAM) and the Materials Research Facility (MRF) at UNT.

## References

[1] D.B. Miracle, High entropy alloys as a bold step forward in alloy development, Nat. Commun. 10 (2019) 1805, doi:10.1038/s41467-019-09700-1.
[2] J.-W. Yeh, S.-K. Chen, S.-J. Lin, J.-Y. Gan, T.-S. Chin, T.-T. Shun, C.-H. Tsau, S.-Y. Chang, Nanostructured high-entropy alloys with multiple principal elements: novel alloy design concepts and outcomes, Adv. Eng. Mater. 6 (2004) 299–303, doi:10.1002/adem.200300567.
[3] B. Cantor, I.T.H. Chang, P. Knight, A.J.B. Vincent, Microstructural development in equiatomic multicomponent alloys, Mater. Sci. Eng. A 375–377 (2004) 213–218, doi:10.1016/j.msea.2003.10.257.
[4] B. Gwalani, V. Soni, D. Choudhuri, M. Lee, J.Y. Hwang, S.J. Nam, H. Ryu, S.H. Hong, R. Banerjee, Stability of ordered L12 and B2 precipitates in face centered cubic based high entropy alloys – Al0.3CoFeCrNi and Al0.3CuFeCrNi2, Scr. Mater. 123 (2016) 130–134, doi:10.1016/j.scriptamat.2016.06.019.
[5] T.-T. Shun, Y.-C. Du, Microstructure and tensile behaviors of fcc Al0.3CoCrFeNi high entropy alloy, Alloys Compd 479 (2009) 157–160, doi:10.1016/j.jallcom.2008.12.088.
[6] M.V. Karpets, O.M. Myslyvchenko, O.S. Makarenko, V.F. Gorban', M.O. Krapivka, Mechanical properties and formation of phases in high-entropy crfenicucoal x alloys, Powder Metall. Met. Ceram. 54 (2015) 344–352, doi:10.1007/s11106-015-9720-9.
[7] H. Zhang, Y. He, Y. Pan, Enhanced hardness and fracture toughness of the laser-solidified FeCoNiCrCuTiMoAlSiB0.5 high-entropy alloy by martensite strengthening, Scr. Mater. 69 (2013) 342–345, doi:10.1016/j.scriptamat.2013.05.020.
[8] M.F. del Grosso, G. Bozzolo, H.O. Mosca, Determination of the transition to the high entropy regime for alloys of refractory elements, J. Alloys Compd. 534 (2012) 25–31, doi:10.1016/j.jallcom.2012.04.053.
[9] C. Ng, S. Guo, J. Luan, S. Shi, C.T. Liu, Entropy-driven phase stability and slow diffusion kinetics in an Al0.5CoCrCuFeNi high entropy alloy, Intermetallics 31 (2012) 165–172, doi:10.1016/j.intermet.2012.07.001.
[10] M.-H. Tsai, J.-W. Yeh, High-entropy alloys: a critical review, Mater. Res. Lett. 2 (2014) 107–123, doi:10.1080/21663831.2014.912690.
[11] M.-H. Tsai, Physical properties of high entropy alloys, Entropy (2013) 15, doi:10.3390/e15125338.
[12] B. Gwalani, S. Gorsse, D. Choudhuri, Y. Zheng, R.S. Mishra, R. Banerjee, Tensile yield strength of a single bulk Al0.3CoCrFeNi high entropy alloy can be tuned from 160 MPa to 1800 MPa, Scr. Mater. 162 (2019) 18–23, doi:10.1016/j.scriptamat.2018.10.023.
[13] Y. Liu, C. Cheng, J. Shang, R. Wang, P. Li, J. Zhao, Oxidation behavior of high-entropy alloys AlxCoCrFeNi ($x = 0.15$, 0.4) in supercritical water and comparison with HR3C steel, Trans. Nonferrous Met. Soc. China 25 (2015) 1341–1351, doi:10.1016/S1003-6326(15)63733-5.
[14] B. Gwalani, V. Soni, M. Lee, S.A. Mantri, Y. Ren, R. Banerjee, Optimizing the coupled effects of Hall–Petch and precipitation strengthening in a Al0.3CoCrFeNi high entropy alloy, Mater. Des. 121 (2017) 254–260, doi:10.1016/j.matdes.2017.02.072.
[15] Y.P. Wang, B.S. Li, M.X. Ren, C. Yang, H.Z. Fu, Microstructure and compressive properties of AlxCoCrFeNi high entropy alloy, Mater. Sci. Eng. A 491 (2008) 154–158, doi:10.1016/j.msea.2008.01.064.
[16] Y.-F. Kao, T.-J. Chen, S.-K. Chen, J.-W. Yeh, Microstructure and mechanical property of as-cast, -homogenized, and -deformed AlxCoCrFeNi ($0 \le x \le 2$) high-entropy alloys, Alloys Compd 488 (2009) 57–64, doi:10.1016/j.jallcom.2009.08.090.
[17] S. Gangireddy, B. Gwalani, V. Soni, R. Banerjee, R.S. Mishra, Contrasting mechanical behavior in precipitation hardenable AlxCoCrFeNi high entropy alloy microstructures: single phase fcc vs. dual phase fcc-bcc, Mater. Sci. Eng. A 739 (2019) 158–166, doi:10.1016/j.msea.2018.10.021.
[18] Z. Li, S. Zhao, H. Diao, P.K. Liaw, M.A. Meyers, High-velocity deformation of Al0.3CoCrFeNi high-entropy alloy: remarkable resistance to shear failure, Sci. Rep. 7 (2017) 42742, doi:10.1038/srep42742.
[19] B. Gwalani, S. Gorsse, D. Choudhuri, M. Styles, Y. Zheng, R.S. Mishra, R. Banerjee, Modifying transformation pathways in high entropy alloys or complex concentrated alloys via thermo-mechanical processing, Acta Mater. 153 (2018) 169–185, doi:10.1016/j.actamat.2018.05.009.
[20] H.Y. Yasuda, K. Shigeno, T. Nagase, Dynamic strain aging of Al0.3CoCrFeNi high entropy alloy single crystals, Scr. Mater. 108 (2015) 80–83, doi:10.1016/j.scriptamat.2015.06.022.
[21] Z.-M. Jiao, S.-G. Ma, G.-Z. Yuan, Z.-H. Wang, H.-J. Yang, J.-W. Qiao, Plastic deformation of Al0.3CoCrFeNi and alcocrfeni high-entropy alloys under nanoindentation, J. Mater. Eng. Perform. 24 (2015) 3077–3083, doi:10.1007/s11665-015-1576-0.
[22] L. Zhang, P. Yu, H. Cheng, H. Zhang, H. Diao, Y. Shi, B. Chen, P. Chen, R. Feng, J. Bai, Q. Jing, M. Ma, P.K. Liaw, G. Li, R. Liu, Nanoindentation creep behavior of an Al0.3CoCrFeNi high-entropy alloy, Metall. Mater. Trans. A 47 (2016) 5871–5875, doi:10.1007/s11661-016-3469-8.
[23] S. Harm-Jan, The additive manufacturing innovation: a range of implications, J. Manuf. Technol. Manag. 28 (2017) 122–143, doi:10.1108/JMTM-06-2016-0081.
[24] D.W. Rosen, Computer-Aided design for additive manufacturing of cellular structures, Comput. Aided. Des. Appl. 4 (2007) 585–594, doi:10.1080/16864360.2007.10738493.
[25] D.D. Lima, S.A. Mantri, C.V. Mikler, R. Contieri, C.J. Yannetta, K.N. Campo, E.S. Lopes, M.J. Styles, T. Borkar, R. Caram, R. Banerjee, Laser additive processing of a functionally graded internal fracture fixation plate, Mater. Des. 130 (2017) 8–15, doi:10.1016/j.matdes.2017.05.034.
[26] T. Fujieda, H. Shiratori, K. Kuwabara, T. Kato, K. Yamanaka, Y. Koizumi, A. Chiba, First demonstration of promising selective electron beam melting method for utilizing high-entropy alloys as engineering materials, Mater. Lett. 159 (2015) 12–15, doi:10.1016/j.matlet.2015.06.046.
[27] H.R. Sistla, J.W. Newkirk, F. Frank Liou, Effect of al/ni ratio, heat treatment on phase transformations and microstructure of AlxFeCoCrNi2-$x$ ($x$=0.3, 1) high entropy alloys, Mater. Des. 81 (2015) 113–121, doi:10.1016/j.matdes.2015.05.027.
[28] J.J. Lewandowski, M. Seifi, Metal additive manufacturing: a review of mechanical properties, Annu. Rev. Mater. Res. 46 (2016) 151–186, doi:10.1146/annurev–matsci-070115-032024.
[29] V. Manvatkar, A. De, T. DebRoy, Heat transfer and material flow during laser assisted multi-layer additive manufacturing, J. Appl. Phys. 116 (2014) 124905, doi:10.1063/1.4896751.
[30] K. Yuan, W. Guo, P. Li, J. Wang, Y. Su, X. Lin, Y. Li, Influence of process parameters and heat treatments on the microstructures and dynamic mechanical behaviors of inconel 718 superalloy manufactured by laser metal deposition, Mater. Sci. Eng. A 721 (2018) 215–225, doi:10.1016/j.msea.2018.02.014.
[31] C.V. Mikler, V. Chaudhary, V. Soni, B. Gwalani, R.V. Ramanujan, R. Banerjee, Tuning the phase stability and magnetic properties of laser additively processed Fe-30at%ni soft magnetic alloys, Mater. Lett. 199 (2017) 88–92, doi:10.1016/j.matlet.2017.04.054.
[32] N. Shamsaei, A. Yadollahi, L. Bian, S.M. Thompson, An overview of direct laser deposition for additive manufacturing; part II: mechanical behavior, process parameter optimization and control, Addit. Manuf. 8 (2015) 12–35, doi:10.1016/j.addma.2015.07.002.
[33] Z. Wang, T.A. Palmer, A.M. Beese, Effect of processing parameters on microstructure and tensile properties of austenitic stainless steel 304 L made by directed energy deposition additive manufacturing, Acta Mater. 110 (2016) 226–235, doi:10.1016/j.actamat.2016.03.019.
[34] V. Ocelík, N. Janssen, S.N. Smith, J.T.M. De Hosson, Additive manufacturing of high-entropy alloys by laser processing, JOM 68 (2016) 1810–1818, doi:10.1007/s11837-016-1888-z.
[35] J.M. Park, J. Choe, J.G. Kim, J.W. Bae, J. Moon, S. Yang, K.T. Kim, J.-H. Yu, H.S. Kim, Superior tensile properties of 1%C-CoCrFeMnNi high-entropy alloy additively manufactured by selective laser melting, Mater. Res. Lett. (2019) 1–7, doi:10.1080/21663831.2019.1638844.
[36] P. Taylor, G.K. Williamson, R.E. Smallman, III. dislocation densities in some annealed and cold-worked metals from measurements on the X-ray debye- scherrer spectrum, Philos. Mag. (2006) 37–41.
[37] F. Peyrouzet, D. Hachet, R. Soulas, P. Godet, Selective laser melting of Al 0 . 3 cocrfeni high-entropy alloy: printability, microstructure, and mechanical properties, Prog. High-Entropy Alloy. 71 (2019) 3443–3451, doi:10.1007/s11837-019-03715-1.
[38] Z.G. Zhu, Q.B. Nguyen, F.L. Ng, X.H. An, X.Z. Liao, P.K. Liaw, S.M.L. Nai, J. Wei, Hierarchical microstructure and strengthening mechanisms of a CoCrFeNiMn high entropy alloy additively manufactured by selective laser melting, Scr. Mater. 154 (2018) 20–24 DOI: https://DOI.org/10.1016/j.scriptamat.2018.05.015 .
[39] Z. Lei, X. Liu, Y. Wu, H. Wang, S. Jiang, S. Wang, X. Hui, Y. Wu, B. Gault, P. Kontis, D. Raabe, L. Gu, Q. Zhang, H. Chen, H. Wang, J. Liu, K. An, Q. Zeng, T.-G. Nieh, Z. Lu, Enhanced strength and ductility in a high-entropy alloy via ordered oxygen complexes, Nature 563 (2018) 546–550, doi:10.1038/s41586-018-0685-y.
[40] O.C. Hellman, J.A. Vandenbroucke, J. Rüsing, D. Isheim, D.N. Seidman, Analysis of three-dimensional atom-probe data by the proximity histogram, Microsc. Microanal 6 (2000) 437–444, doi:10.1007/S100050010051.
[41] J.M. Hyde, E.A. Marquis, K.B. Wilford, T.J. Williams, A sensitivity analysis of the maximum separation method for the characterisation of solute clusters, Ultramicroscopy 111 (2011) 440–447, doi:10.1016/j.ultramic.2010.12.015.
[42] L.T. Stephenson, M.P. Moody, P.V. Liddicoat, S.P. Ringer, New techniques for the analysis of fine-scaled clustering phenomena within atom probe tomography (APT) data, Microsc. Microanal. 13 (2007) 448–463, doi:10.1017/S1431927607070900.
[43] B. Gwalani, R. Salloom, T. Alam, S.G. Valentin, X. Zhou, G. Thompson, S.G. Srinivasan, R. Banerjee, Composition-dependent apparent activation-energy and sluggish grain-growth in high entropy alloys, Mater. Res. Lett. 7 (2019) 267–274, doi:10.1080/21663831.2019.1601644.
[44] U.F. Kocks, H. Mecking, Physics and phenomenology of strain hardening: the fcc case, Prog. Mater. Sci. 48 (2003) 171–273.
[45] A. Haglund, M. Koehler, D. Catoor, E.P. George, V. Keppens, Polycrystalline elastic moduli of a high-entropy alloy at cryogenic temperatures, Intermetallics 58 (2015) 62–64, doi:10.1016/j.intermet.2014.11.005.
[46] J. Liu, Y. Jin, X. Fang, C. Chen, Q. Feng, X. Liu, Y. Chen, T. Suo, F. Zhao, T. Huang, H. Wang, X. Wang, Dislocation strengthening without ductility trade-off in metastable austenitic steels, Sci. Rep. (2016) 1–10, doi:10.1038/srep35345.
[47] Z. Guo, W. Sha, Quantification of precipitation hardening and evolution of precipitates, Mater. Trans. 43 (2002) 1273–1282, doi:10.2320/matertrans.43.1273.
[48] N. Kumar, M. Komarasamy, P. Nelaturu, Z. Tang, P.K. Liaw, R.S. Mishra, Friction stir processing of a high entropy alloy Al0.1CoCrFeNi, JOM 67 (2015) 1007–1013, doi:10.1007/s11837-015-1385-9.
[49] A.J. Ardell, Precipitation hardening, Metall. Trans. A 16 (1985).
[50] T. Yang, Y.L. Zhao, Y. Tong, Z.B. Jiao, J. Wei, J.X. Cai, X.D. Han, D. Chen, A. Hu, J.J. Kai, K. Lu, Y. Liu, C.T. Liu, Multicomponent intermetallic nanoparticles and superb mechanical behaviors of complex alloys, Science 80 (2018) 1–6.